REVEALING THE INFLUENCE OF DEFINITE BRAIN REGIONS UPON THE EMERGENCE OF SPATIAL AND TEMPORAL PATTERNS IN THE RESTING-STATE BRAIN ACTIVITY

By

Sergei D. Verzilin

THESIS

Submitted in partial fulfillment of the requirements for the degree
MASTER IN BRAIN AND COGNITION
Department of Information and Communication Technologies
Universitat Pompeu Fabra Barcelona

Advisor:
Gustavo Deco
ICREA Full Professor and Research Professor
Director of the Center of Brain and Cognition &
Head of CNS research group
Department of Information and Communication Technologies
Universitat Pompeu Fabra Barcelona

Barcelona, September 2015

Contents

Abstract

The resting-state brain activity exhibits stable spatial and temporal patterns of well-structured coherence between different brain regions. We used a whole-brain model applying the normal form of the Hopf bifurcation for clarification of the roles that different brain regions play in the emergence of the patterns. For this purpose we worked out methods for suppression of model nodes representing different brain regions. We conducted simulation experiments with different groups of nodes suppressed in alternative modes of suppression.

Via comparative analysis of the results obtained in the experiments we distinguished nodes and corresponding brain regions acting as generators of coherent activity or as inter-node transmitters. These nodes played a critical role in patterns emergence. We also observed nodes acting as best recipients of the signals coming from the other nodes.

1. Introduction

In a resting state a person is awake, in static, free from any tasks. The patterns of the resting-state brain activity are distinguishable from patterns observed during sleeping or goal-directed behavior (G. Deco et al., 2013a).

Correlative activity between brain voxels in a resting state define so-called resting state networks.

The analysis of the blood-oxygen-level depended (BOLD) signal obtained in functional magnetic resonance imaging (fMRI) is a verifiable and comprehensible approach to understanding resting state networks through significant amount of empirical data (J. Cabral, M. L. Kringelbach, G. Deco, 2014).

We used the empirical data acquired at Berlin Center for Advanced Imaging, Charité University Medicine, Berlin, Germany. The data were collected from 24 subjects, healthy young men and women (12 males, 12 females, minimal age was 18 years, maximal age was 33, mean 25.7).

The empirical data included standard fMRI BOLD signal time series and individual anatomical brain characteristics obtained via diffusion weighted/tensor imaging methods (DTI) (Basser and Pierpaoli 1996, Beaulieu 2002). Both fMRI and DTI data components conformed to 68 brain regions enumerated in Table 1.

Table 1. Anatomical labels for the 68 parcellated brain regions. The two region numbers per line refer to right and left hemisphere respectively.

Region number	Region name
1;35	Banks superior temporal sulcus
2;36	Caudal anterior cingulate cortex
3;37	Caudal middle frontal gyrus
4;38	Cuneus cortex
5;39	Entorhinal cortex
6;40	Fusiform gyrus
7;41	Inferior parietal cortex
8;42	Inferior temporal gyrus

Region number	Region name
9;43	Isthmus cingulate cortex
10;44	Lateral occipital cortex
11;45	Lateral orbital frontal cortex
12;46	Lingual gyrus
13;47	Medial orbital frontal cortex
14;48	Middle temporal gyrus
15;49	Parahippocampal gyrus
16;50	Paracentral lobule
17;51	Pars opercularis
18;52	Pars orbitalis
19;53	Pars triangularis
20;54	Pericalcarine cortex
21;55	Postcentral gyrus
22;56	Posterior cingulate cortex
23;57	Precentral gyrus
24;58	Precuneus cortex
25;59	Rostral anterior cingulate cortex
26;60	Rostral middle frontal gyrus Superior frontal gyrus
27;61	Superior frontal cortex
28;62	Superior parietal cortex
29;63	Superior temporal gyrus
30;64	Supramarginal gyrus
31;65	Frontal pole
32;66	Temporal pole
33;67	Transverse temporal cortex
34;68	Insula

Bold signals were recoded during subjects' resting state condition (awake, eyes closed, no task to be performed). Sampling rate was one frame per two seconds. We had a dataset of size 68x661, i.e. 661 frames recoded for all the 68 brain regions during 22 minutes for all the 24 subjects.

Individual spatial configuration of 68 brain regions (inter-region distance) was reconstructed for each subject from the DTI data with the aid of probabilistic tractographic methods (Johansen-Berg and Rushworth (2009), Hagmann, P., L. Cammoun, et al, 2010).

Individual spatial configurations were arranged in a form of the 24 68x68 connectivity matrices according to (Schirner, Rothmeier, et al., Ritter, Schirner, et al., 2013).

Individual connectivity matrices and subjects' BOLD signal time series constitute the empirical datasets we used for the model verification.

We proclaim the goal of modeling as a search for basic mechanisms producing spatial and temporal patterns in the resting-state brain activity. This goal necessitates determination of such common features in individual datasets that are important for an emergent of patterns.

A simple analysis of empirical datasets provides reasoning for main approaches to model construction and adjustment.

Direct comparison of individual BOLD signal time series shows sufficient variety of subjects' datasets. We performed the standard one-way analysis of variance (one-way ANOVA) for every of the 68 brain regions taking signal value as a dependent variable and a subject ownership of a time series as an independent factor. Figure 1 in Annex 1 shows the ANOVA results.

Fortunately, we can obtain reliable spatial and temporal patterns of the resting-state brain activity. Such patterns are common for all subjects and can be described in a uniform way. The most simple and well-understood spatial pattern is the functional connectivity (FC) expressing correlation between brain regions (see Deco, Jirsa, 2011, Deco, Jirsa, et al., 2013b) Schirner, Rothmeier, et al., Ritter, Schirner, et al., 2013).

We calculated individual FC as 68x68 matrices taking BOLD signal time series for each pair of brain regions. Then we evaluated the similarity of individual FC patterns. For that purpose we obtainend inter-subject correlations for samples consisting of FC elements below the main diagonal. Each sample was of the size (68x68-68)/2=2278.

Thus we calculated a 24x24 correlation matrix. All correlations appeared to be statistically significant. The minimal correlation was 0.3494, the maximal one was equal to 0.8374, while the mean value was 0.598. We can conclude that the level of similarity for individual FC patterns is rather high.

Now we can formulate the main approches to model construction and adjustment.

1. The most evident conclusion bear on the directions of modeling we should avoid rather than on the directions we should accept. Clearly, trying to simulate individual BOLD signal time series and especially some average time series is meaningless.

2. Instead of linking to particular time series we need to consider cause-effect relations between activities in different brain regions. The model should produce spatial and temporal patterns emerging from those relations.

3. Similarly, adaptation of model parameters should be qualified through metrics expressing conformity of simulated patterns to empirical ones. More spatial patterns and some temporal patterns will be considered below.

2. Methods

2.1. Empirical data processing

2.1.1. Averaging and normalization

As far as we aim to obtain common factors arousing the emergence of brain-activity patterns, then the most simple and reasonable way to use all individual connectivity data is to bring into models mean connectivity and functional connectivity matrices. Thus we calculated simple average values for each element of the FC matrix summing over subjects and dividing by the total number of subjects (24). We can get the same results in a different way. We may normalize each individual time series and then arrange a united sample consisting of 24 normalized individual datasets. Obviously, we would get the

same average FC matrix calculating correlation through the united sample. We can normalize and bring together datasets whenever an affine transformation of a sample does not change the characteristics to be obtained.

Besides of correlations that condition pertains to characteristics of BOLD-signal spectrums.

2.1.2. Spectrum processing

We analyzed spectrums applying signal filtering of empirical BOLD signals for three purposes. First, we found out prevailing frequencies of signals at different brain regions. Second, we estimated a proportion of a spectrum power at a target frequency band of 0.04 – 0.07 Hz known to be most functionally relevant (Biswal, Yetkin, et al., 1995). Third, we considered a phase shift of signals at different brain regions and an altering of the phase shift.

We used two bandpass filters. The first band covered BOLD-signal spectrum from 0.04 Hz to the Nyquist frequency equal to 0.25 Hz. It was defined as sampling rate (1 frame per 2 seconds) divided by 2. The second was the above mentioned target band of 0.04 – 0.07 Hz.

We used the Butterworth filter to get a flat amplitude response (Butterworth, 1930)). To compensate a phase distortion we performed the bi-directional filtering (Smith, 1997). The details of filtration and spectrum smoothing are presented in Annex 2.

2.2. Model adjustment

2.2.1. Whole-brain model

The whole brain model corresponds to the structure and contents of the empirical data. It reveals a mutual interaction of the local brain activity in 68 model nodes corresponding to the 68 brain regions. The model describes a neural mass activity via a normal form of a Hopf bifurcation (Freyer, Roberts, et al., 2011, 2012). This form lets identify each node to be asynchronius or oscilatory depending on a bifurcation parameter.

The local activity of each node j is described by the real part x_j of the complex variable z_j in the following equation:

$$dz_j/dt = [a_j + i\omega_j - |z_j|^2]z_j + \beta\eta_j(t), \quad (1)$$

where $z_j = \rho_j \exp(i\Theta_j) = x_j + iy_j$

and $\beta\eta_j(t)$ is an additive Gauss noise with a standart deviation β. In the adjusted model we used $\beta=0.02$. Here a_j is a parameter specifying whether node j is asynchronous with random fluctuations around the stable value $z_j=0$ at $a<0$, or synchronous at $a>0$, while $a_j=0$ is a state of a supercritical bifurcation. At the synchronous mode node j gets a stable limit cycle such that the variable z oscillates wth an intrinsic frequency of $\nu_j = \omega_j/2\pi$. The inter-node interaction depends on the connectivity matrix C described above. The following couple of differential equations incorporate mutual interaction of nodes.

$$dx_j/dt = [a_j - x_j^2 - y_j^2]x_j - \omega_j y_j + G\sum_i C_{ij}(x_i - x_j) + \beta\eta_j(t) \quad (2)$$

$$dy_j/dt = [a_j - x_j^2 - y_j^2]y_j - \omega_j x_j + G\sum_i C_{ij}(y_i - y_j) + \beta\eta_j(t) \quad (3)$$

Where G is a global connectivity parameter.

In our research we used first-order Euler method to handle differential equations. That reduced the simulation time and provided suitable accuracy for obtaining spatial and temporal patterns of the resting-state brain activity. The global parameter G and the parameters ω_j and a_j introduced for each node j were to be identified in order to improve metrics of model quality.

2.2.2. Metrics of model quality

Functional connectivity

The model should produce a reasonably good approximation of the average empirical functional connectivity matrix (FC) described above. We used values of variables x_j in the equations (5)-(6) for each node j at different time points to calculate a simulated functional connectivity matrix SFC. Then we repeated the same approach we exploited for comparison of individual subjects' functional connectivity matrices. Thus, the metric "FC Fitting" for the model quality regarding simulation of the functional connectivity is the correlation between two samples consisting of respective elements of FC and SFC below the main diagonal.

Functional connectivity dynamics

To consider temporal patterns of the functional connectivity we calculated so-called functional connectivity dynamics matrices (FCD) (Hansen, Battaglia, et al., 2015). For that we calculated FC matrices for 61 windows each of which contained 30 sequential observations. Proximate windows contained 20 common observations. In other words, each window lasted one minute and proximate windows overlaped by 40 seconds.

Thus we got 61 empirical FC matrices for each of the 24 subjects. Taking elements below the main diagonal we calculated 24 inter-window corelations obtaining 24 61x61 FCD matrices. Then we arranged a sample containing 24*(61*61-61/2) = 43920 subdiagonal elements of the 24 FCD matricts.

In a similar way we got 24 simulated FCD matrices and arranged a simulated saple of the same size (43920 elements).

In order to measure the ability of the model to describe temporal FC patterns we compared the two samples.

More exactly, we compared two distribution functions applying the non-parametric Kolmogorov-Smirnov criteria to the samples. The distance "KS distance" generated in the Kolmogorov-Smirnov test was used as a quality metric.

Metastability

We analyzed phase synchronization between different nodes and fluctuations of such synchronization. The "Metastability" is a metric characterizing the level of fluctuations in the inter-node synchronization (Wildie, Shanahan, 2012). We expected fluctuations not to be high. We calculated the metastability as the

standart deviation (across time) of the Kuramoto order parameter. The Kuramoto order parameter can be defined as follows:

$$R(t) = |\sum_{j=1...N} exp(i*\varphi_j(t))|/N, \quad (4)$$

where $\varphi_j(t)$ is a phase of a filtered signal for the bandpass 0.04 .. 0.07 at node j.

The Kuramoto order parameter is a measure of the inter-node synchronization varying from 0 (copletly independent phases) to 1 (full) synchonization. We computed phases $\varphi_j(t)$ for filtered signals at each node j via the Hilbert transform H [V. Alan, 1998].

The Hilbert transform produced an imaginary component for a real-value signal $x_j(t)$ at node j:

$$z_j(t) = x_j(t) + i*H[x_j(t)] \quad (5)$$

The phase $\varphi_j(t)$ at each node j and time t can be determined as follows:

$$\varphi_j(t) = arccos[x_j(t)/ |z_j(t)|] \text{ for } H[x_j(t)] >= 0, \quad (6)$$

$$\varphi_j(t) = 2\pi - arccos[x_j(t)/ |z_j(t)|] \text{ for } H[x_j(t)] < 0. \quad (7)$$

We can use equation (7) to calculate the Kuramoto order parameter at each time t and then we can obtain the metric "Metastability" as a standard deviation across time.

Additional metrics

Here we introduce two additional metrics, namely "Integration" and "Mean Synchronization". We do not use these metrics for the model adjustment, but use them together with the other ones in further experiments.

$$Integration = \int_0^1 SA(p))dp / size(FC) \quad (8)$$

$$A(p) = [(|FC - E| - I*p) > 0], \quad (9)$$

i.e. the matrix $A(p)$ contains the elements *1=true* and *0=false* according to the fulfillment of the inequality in (9).

Here FC is a functional connectivity matrix; E is an identity matrix; I is a matrix of ones (the two latter have the same size as FC); $S(A(p))$ is the size (the number of elements) of the maximal component for the connectivity matrix $A(p)$; $size(FC)$=68.

Mean synchronization is calculated as a mean value of the Kuramoto oder parameter (7) across time.

2.2.3. Model parameters identification

We identified model parameters comprised of the frequency parameter ω_j for each node j, bifurcation parameter a_j for each node j, and the global parameter G in three respective stages. The most simple and evident method was used at the first stage for calculation of frequency parameters ω_j, $j=1$ .. 68. We considered an average (across 24 subjects) filtered with a bandpass 0.04…0.07Hz one-sided smoothed amplitude spectrums at each node j. All details of filtering, spectrum evaluation and smoothing were described above and in Annex 2. Then we found prevailing frequencies ν_j, j = 1..68 with maximal amplitudes. And finally we got $\omega_j = 2\pi\nu_j$, j = 1..68.

At the second stage we evaluated the bifurcation parameter a_j for each node j. We targeted to simulate the empirical average proportion of an absolute power amount within the band 0.04 …0.07 Hz to that within the band 0.04 …0.25 Hz at each node j:

$$p_j = \int_{0.04}^{0.07} P_j(f)df \,/\, \int_{0.04}^{0.25} P_j(f)df \tag{10}$$

As nodes activities influence each other, we used an iterative descendent strategy to update all 68 parameters simultaneously:

$$a_j = a_j + \eta(p_j^{empirical} - p_j^{simulated}) \tag{11}$$

until convergence.

We must note that p_j is an increasing function of a_j, $j=1...N$, hence we need not define a general goal function for all nodes and calculate its exact gradient. We used η=0.1.

We got the difference between empirical and simulated proportion (normalized to the empirical proportion) less than 0.01 for all nodes.

Figure 1 illustrates the results of the bifurcation parameters selection.

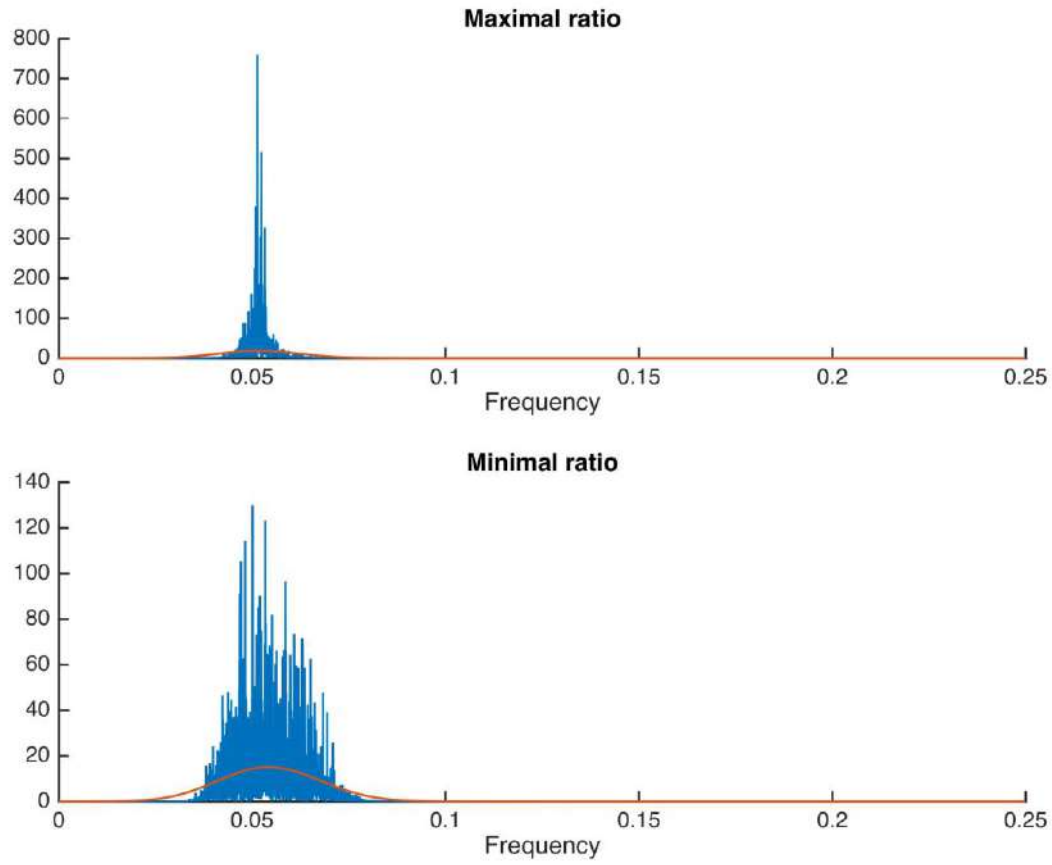

Figure 1. Power spectrums. The filtered simulated spectrums and smoothed spectrums for two nodes (with the best ratio fitting the empirical data and the worst one) are shown here.

At the third stage we obtained reasonable values for the global parameter G taking into account three metrics introduced above.

We determined the interval from 3 to 6 to be the most suitable to take the value of G from (see Figure 2.)

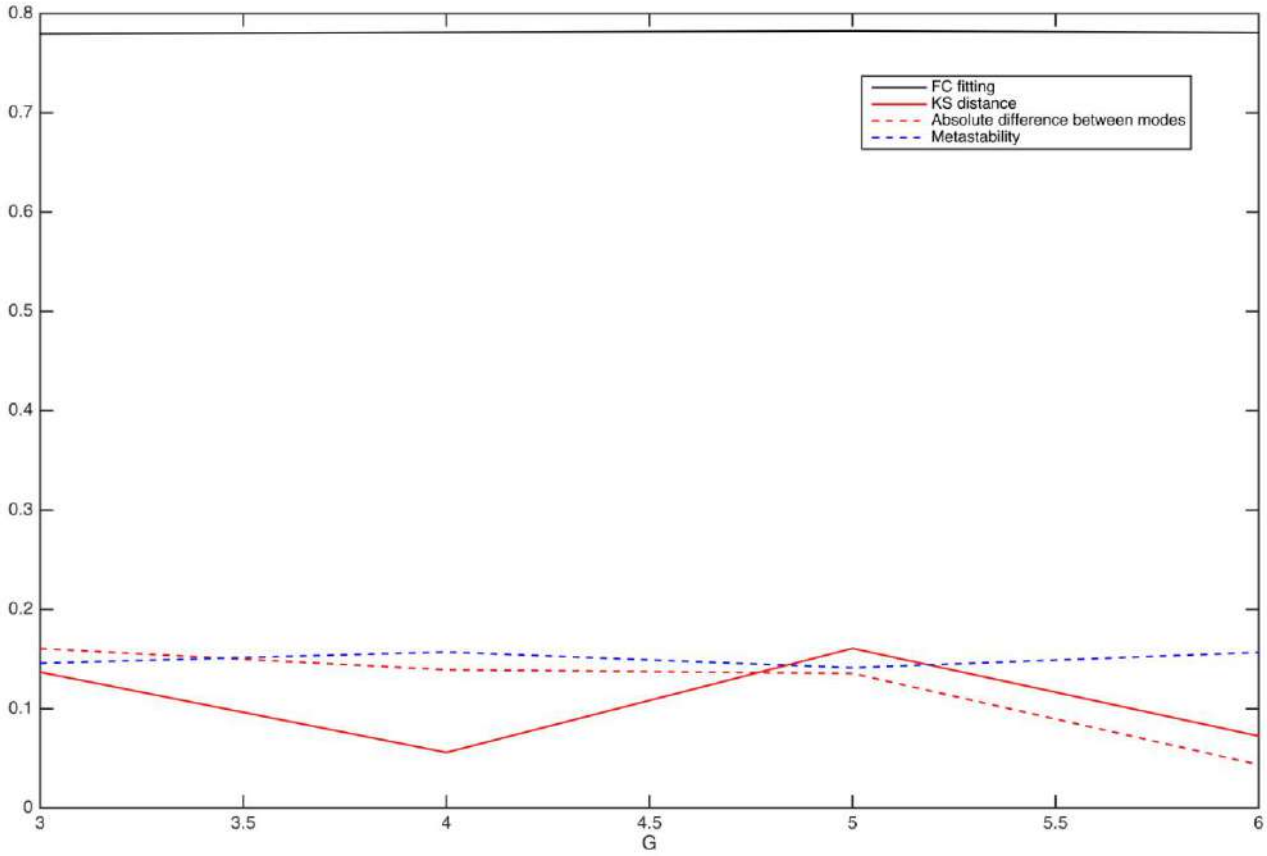

Figure 2. The values of quality metrics subject to the global parameter *G*. Here FC fitting is a metric for quality of FC simulation; KS distance is a distance obtained in the Kolmogorov-Smirnov test applied to simulated and empirical FCD matrices. Absolute difference between nodes is an additional characteristic for the same distributions as in the Kolmogorov-Smirnov test. Metastability is a standard deviation across the time of fluctuation on the inter-node synchronization.

We performed a more detailed analysis of the fitting for G=4.5.

The regression analysis was used to control the accuracy of functional connectivity data (FC_{simul}) obtained via the simulation as compared with the empirical functional connectivity (FC_{emp}).

We regarded FC_{simul} as a depended variable and FC_{emp} as an independent variable in the linear regression model:

$$FC_{simul} = b_0 + b_1 * FC_{emp} + Error. \quad (12)$$

Table 2 contains regression summary, and Figure 3 shows the scatter chart with the regression line.

Table 2. Regression summary

Estimated Coefficients:				
	Estimate	*SE*	t_{Stat}	*p-value*
b_0 *(Intercept)*	-0.078373	0.008877	-8.8288	2.0663e-18
b_1	1.1037	0.018468	59.762	0
Number of observations: 2278, Error degrees of freedom: 2276 Root Mean Squared Error: 0.129 *R*-squared: 0.611, Adjusted *R*-Squared 0.611 *F*-statistic vs. constant model: 3.57e+03, *p-value* could not be distinguished from 0.				

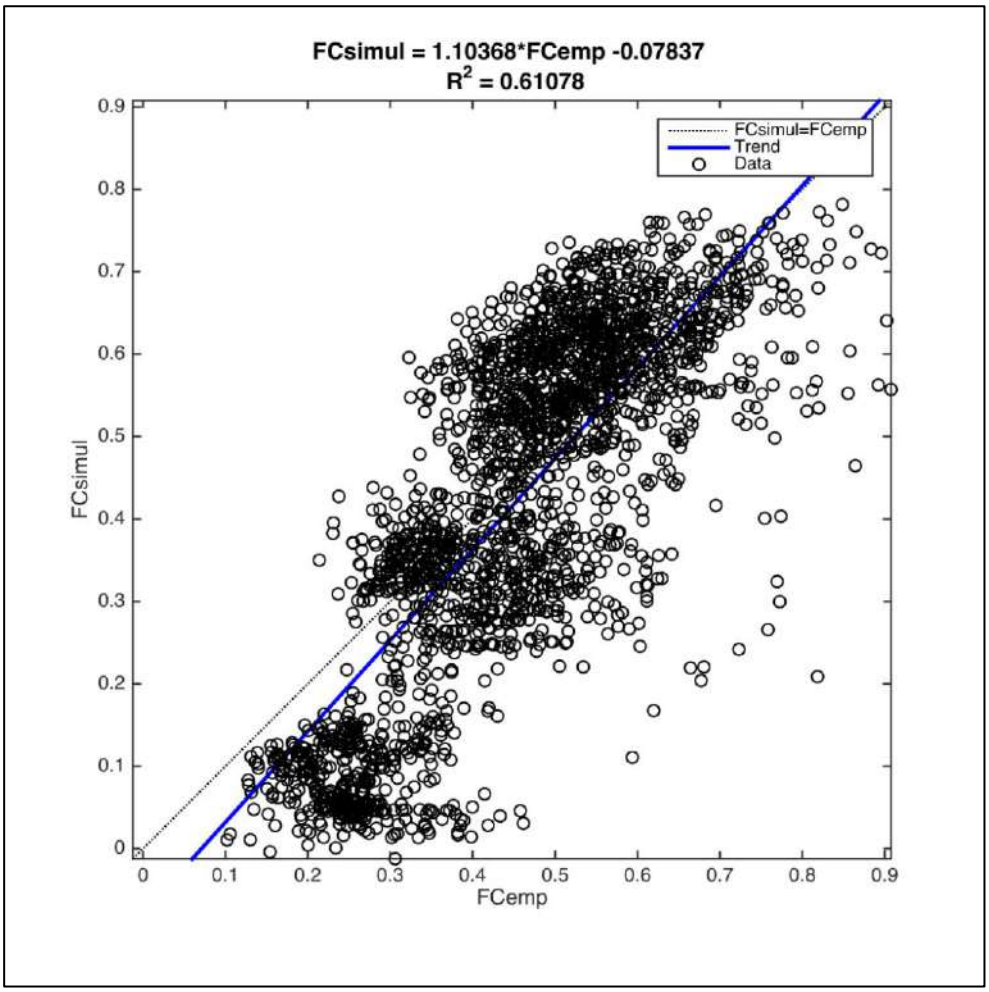

Figure 3. Scatter chart. According to the value of *R*-squared, the regression accounted for 61% of the variance in the FC_{simul} data, while the correlation of FC_{simul} and FC_{emp} was equal to 0.782. The latter value was regarded as an acceptable fitting characteristic for the model functional connectivity.

Figure 3 also shows the dotted line representing the ideal regression with $b_0=0$ and $b_1=1$. Though the deviation of b_0 from zero is statistically significant (P=2.0663e-18), the absolute value of deviation is not big (less than 0.1). Similarly the value of b_1 is close to 1. Thus not only the fitting characteristic, but also the results of regression analysis show the accuracy suitable for simulation purposes.

However we can see slightest specific of simulated *FC* distribution: we have got gaps at the correlation values near 0.2 and 0.43, while no gaps can be seen for the empirical data.

Figure 4 shows colored versions of absolute (positive) *FC* and *SFC* matrices.

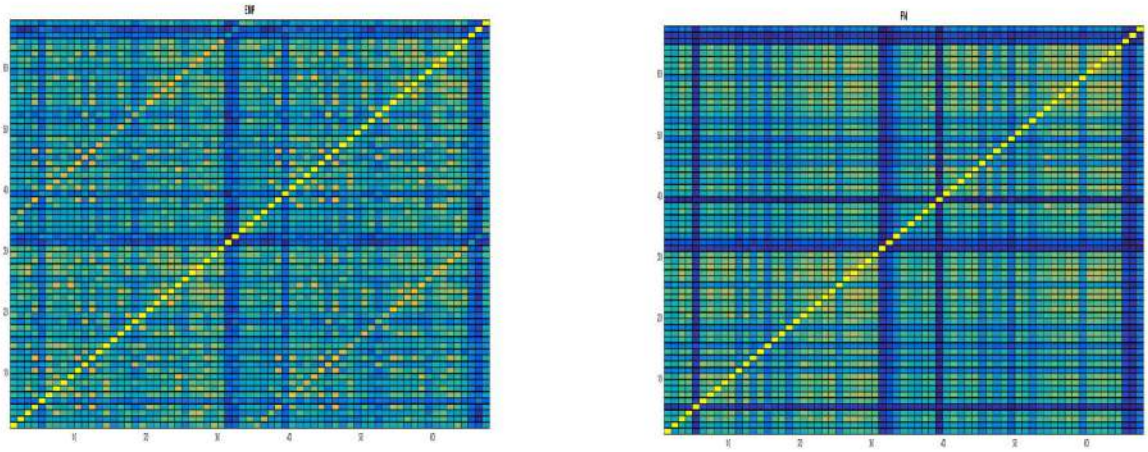

FC *SFC*

Figure 4. *FC* and *SFC* matrices. We used the blue-green-yellow palette from dark blue (close to zero correlations) to bright yellow (high positive correlations). Here the matrices are transposed: the elements are enumerated from the south-west corner. The differences between two pictures are attributed to high empirical correlations obtained for symmetrical nodes in the left and right hemisphere (nodes 2 and 36, 4 and 38, 6 and 40, etc.). The model could not display that effect.

2.3. Nodes suppression

The adjusted model was used in order to find nodes and factors significant for emergence of spatial and temporal patterns in the resting-state brain activity.

In our experiments we suppressed different groups of nodes and examined alteration of patterns' characteristics. We used three methods for nodes suppression, namely: isolating, deleting, and freezing.

The isolating method changed the empirical connectivity matrix in such a way that the rows and columns corresponding to the suppressed nodes contained zero elements.

The deleting method reduced the size of matrices and vectors by the number of nodes deleted.

More properly, the deleting method, as compared with the isolating method, does not change the modeling processes but influences the calculation of the model metrics.

The freezing method substituted the bifurcation parameters of the nodes suppressed for a minimal (across all nodes) value.

3. Results

3.1. Criteria for Nodes Selection

We conducted modeling with different groups of nodes suppressed comparing output values of the metrics introduced above (FC Fitting, KS Distance, Metastability, Integration, Mean Synchronization).

We formed the groups of nodes to be suppressed according to the bifurcation parameters a_i and the values of the connectivity rate c_i calculated for each node $i=1,\ldots,68$ as a sum over column or row i in the connectivity matrix C.

All the data used for nodes selection are placed in the Table 3.

Table 3. Data for nodes selection

Node Number	Rank *a*	*a*	Rank |*a*|	|*a*|	Rank *c*	*c*
1	55	0.2028	32	0.2028	21	0.1360
2	42	0.0816	10	0.0816	14	0.0867
3	59	0.2474	38	0.2474	45	0.3914
4	54	0.2012	31	0.2012	22	0.1363
5	21	-0.2824	39	0.2824	2	0.0138
6	16	-0.3834	49	0.3834	39	0.3021
7	13	-0.4489	54	0.4489	61	0.6959
8	2	-1.5562	67	1.5562	46	0.3977
9	63	0.3421	47	0.3421	32	0.2064
10	47	0.1410	19	0.1410	56	0.5343
11	6	-0.7665	63	0.7665	24	0.1430
12	67	0.4643	55	0.4643	36	0.2156
13	39	0.0364	5	0.0364	15	0.0966
14	11	-0.4957	58	0.4957	47	0.3982
15	31	-0.1164	14	0.1164	7	0.0378
16	51	0.1769	27	0.1769	25	0.1512
17	50	0.1686	26	0.1686	41	0.3227
18	28	-0.1448	20	0.1448	13	0.0807
19	64	0.3831	48	0.3831	31	0.1973
20	49	0.1674	24	0.1674	33	0.2073
21	65	0.3965	50	0.3965	48	0.4009
22	40	0.0607	7	0.0607	26	0.1589
23	32	-0.0962	12	0.0962	62	0.7130
24	57	0.2164	34	0.2164	54	0.5147
25	41	0.0783	9	0.0783	12	0.0704
26	20	-0.2870	40	0.2870	60	0.6825
27	4	-1.1397	65	1.1397	68	1.1589
28	22	-0.2458	37	0.2458	65	0.7897
29	5	-1.0171	64	1.0171	52	0.4753
30	10	-0.4982	59	0.4982	58	0.5451
31	24	-0.1933	30	0.1933	3	0.0143
32	23	-0.2355	36	0.2355	6	0.0270
33	38	0.0107	1	0.0107	10	0.0487
34	29	-0.1349	16	0.1349	40	0.3023
35	53	0.1888	29	0.1888	23	0.1407
36	45	0.1356	17	0.1356	17	0.1053
37	43	0.0844	11	0.0844	44	0.3777
38	52	0.1784	28	0.1784	19	0.1310
39	19	-0.3123	43	0.3123	1	0.0100
40	14	-0.4386	53	0.4386	38	0.2931
41	15	-0.4203	51	0.4203	64	0.7750

Node Number	Rank *a*	*a*	Rank |*a*|	|*a*|	Rank *c*	*c*
42	1	-1.7865	68	1.7865	42	0.3498
43	60	0.2879	41	0.2879	30	0.1959
44	61	0.2965	42	0.2965	53	0.4938
45	9	-0.6454	60	0.6454	20	0.1355
46	66	0.4384	52	0.4384	35	0.2137
47	44	0.1111	13	0.1111	18	0.1104
48	7	-0.6724	62	0.6724	50	0.4206
49	25	-0.1685	25	0.1685	9	0.0431
50	58	0.2261	35	0.2261	28	0.1739
51	48	0.1552	21	0.1552	37	0.2611
52	30	-0.1333	15	0.1333	16	0.1024
53	62	0.3403	46	0.3403	34	0.2122
54	56	0.2104	33	0.2104	29	0.1844
55	68	0.4829	57	0.4829	49	0.4157
56	46	0.1382	18	0.1382	27	0.1609
57	34	-0.0475	6	0.0475	63	0.7218
58	35	-0.0290	4	0.0290	57	0.5370
59	37	-0.0120	2	0.0120	11	0.0652
60	26	-0.1621	23	0.1621	59	0.6813
61	3	-1.3580	66	1.3580	67	1.1055
62	12	-0.4682	56	0.4682	66	0.8470
63	8	-0.6474	61	0.6474	51	0.4526
64	33	-0.0703	8	0.0703	55	0.5154
65	27	-0.1600	22	0.1600	4	0.0216
66	18	-0.3198	44	0.3198	5	0.0225
67	36	-0.0160	3	0.0160	8	0.0385
68	17	-0.3330	45	0.3330	43	0.3688

Here node number correspond to numeration used above in Table 1, columns *a*, |*a*|, contain respectively bifurcation parameters and their absolute values, column *c* contains connectivity rates. Ranks were obtained for corresponding characteristics by sorting them in ascending order.

We can see a strong relationship between bifurcation parameters in symmetrical nodes corresponding to brain regions of right (1…34) and left (35…68) hemispheres. This relationship was confirmed via the regression analysis with the results summarized in Figure 5.

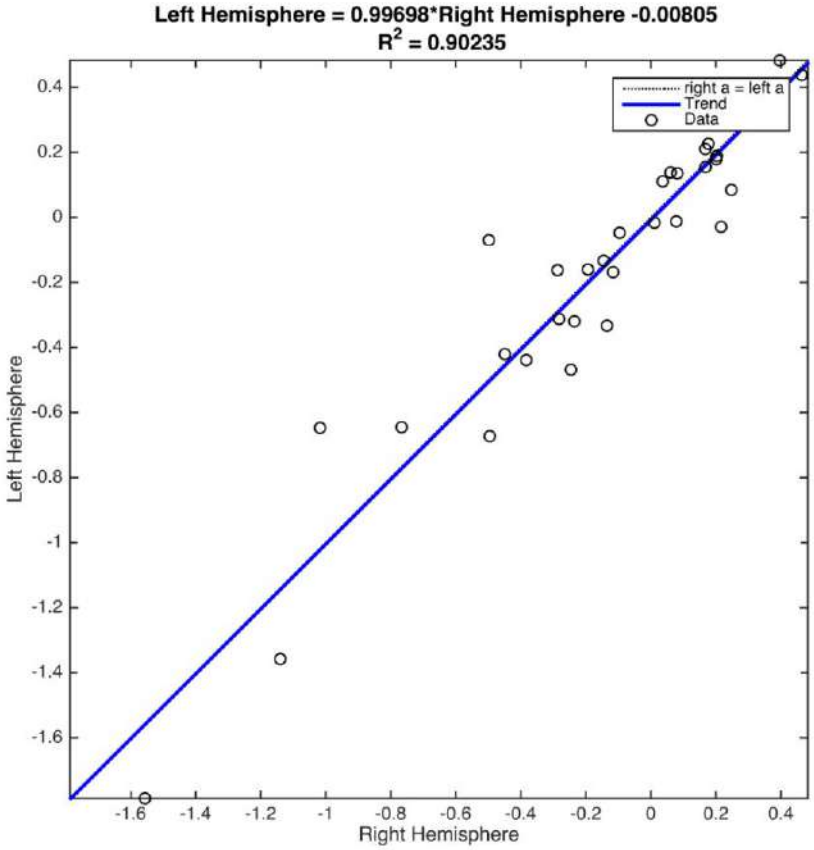

Figure 5. Regression for bifurcation parameters in nodes corresponding to symmetrical brain regions of left and right hemispheres. We can see that the trend almost coincides with the identical function graph with squared R greater than 0.9. Recalling the procedure of parameters identification we can conclude that the source of the regression lays in similarity of spectrums in symmetrical brain regions.

The link between symmetrical nodes was considered for selection of nodes with specific characteristics for additional experiments.

We used the data in Table 3 to establish the criteria of nodes selection and to generate corresponding groups of suppressed nodes: nodes with bifurcation parameters close to zero (BC); nodes with the lowest bifurcation parameters (LBC); nodes with the highest bifurcation parameters (HBC); nodes with the highest connectivity rate (RC); nodes with the lowest connectivity rate (NRC).

3.2. General Results for Suppressed Groups of Nodes

Here we analyze the results of experiments carried out for four groups of suppressed nodes (BC, RC, LBC, HBC). We also considered the empirical data (EMP) and the results of modeling with the full set of nodes (FN). All simulated data were obtained for the global connectivity parameter G=4.5. We used isolating and freezing methods (see Methods) of nodes suppression.

Figure 6 shows functional connectivity (FC) matrices for ten variants of data specified above.

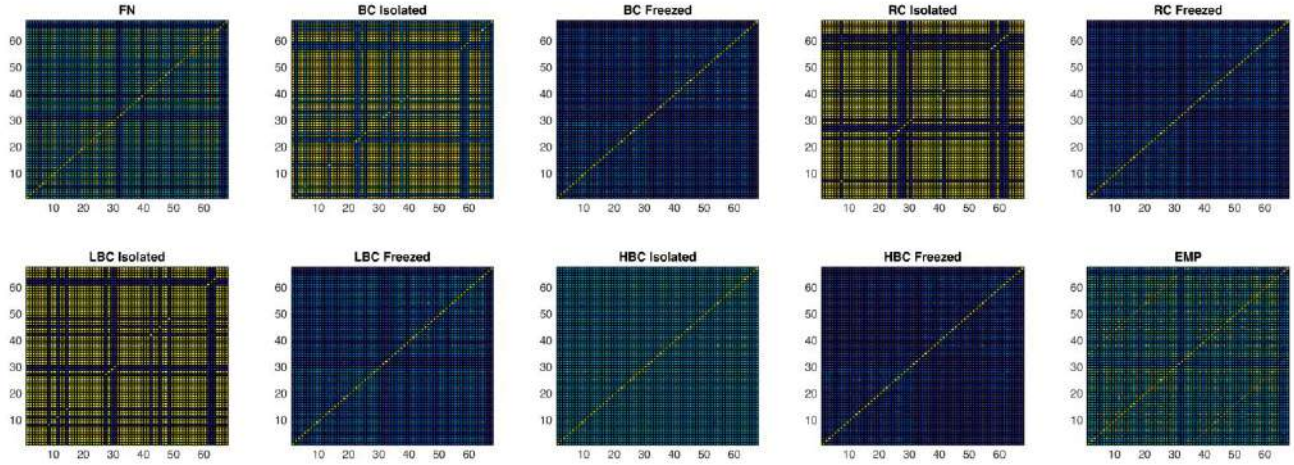

Figure 6. FC matrices. FC matrices are displayed in the blue-green-yellow palette (similarly to Figure 4 see Methods) from dark blue (close to zero correlations) to bright yellow (high positive correlations). The matrices are transposed as the elements are enumerated from the south-west corner. We can see dark stripes at every picture corresponding to data with isolated nodes. These stripes show close-to-zero correlations of time series in the isolated nodes.

We used the deleting method (see Methods) to exclude the effect of zero correlations in the value of the FC Fitting metric. The values of the metrics for ten variants of data can be found in the Table 4 below. The considerations about the influence of different groups of nodes upon the functional connectivity patterns are presented in the comments to the table.

Figure 7 shows functional connectivity dynamics matrices (FCD) for the same ten variants of data.

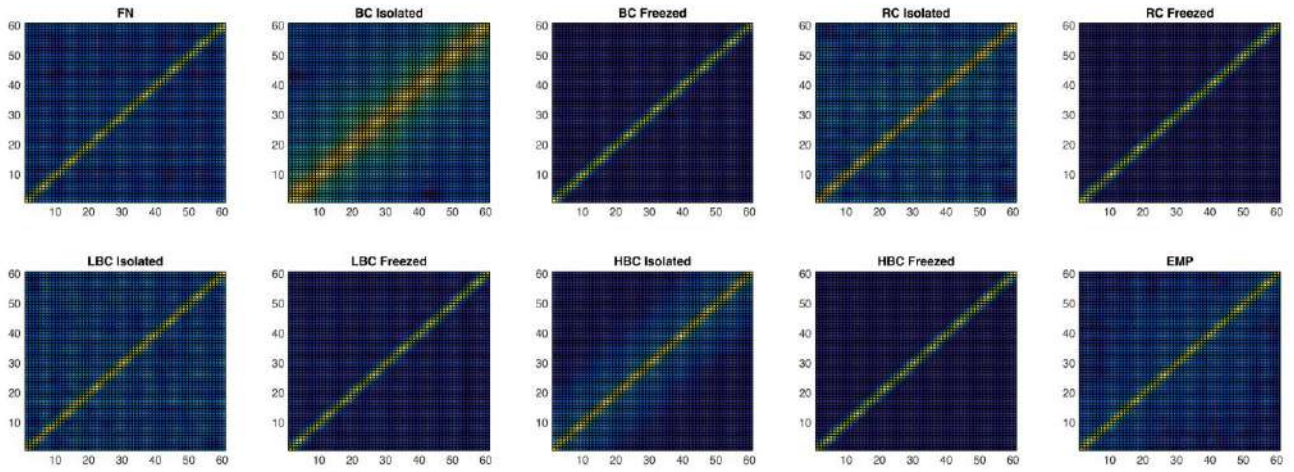

Figure 7. FCD matrices. We used the same palette as in the previous figure. When comparing pictures of different FCD matrices we should keep in mind that the KS Distance metric, as distinct from the FC Fitting, depends on distribution of colons, rather than on the position of spots.

For more precise analysis of FC and FCD patterns we put together the exact values of FC Fitting and KS Distance metrics are in Table 4.

Table 4. FC Fitting and KS distance metrics

	FN	BC	RC	LBC	HBC	EMP
Freezing						
FC Fitting	0.7838	0.6772	0.6831	0.7460	0.5730	1
KS Distance	0.0535	0.8665	0.9091	0.7762	0.9286	0
Isolating						
FC Fitting	0.7838	0.2463	-0.1606	-0.1408	0.3871	1
KS Distance	0.0535	0.5844	0.9184	0.9823	0.7623	0
Deleting						
FC Fitting	0.7838	0.7816	0.5465	0.5224	0.6969	1
KS Distance	0.0535	0.4670	0.8774	0.9065	0.8665	0

All the differences between values of the FC Fitting metric are statistically significant because of the large sizes ((68*68-68)/2=2278) of the samples consisting of the subdiagonal elements of the FC matrices (we calculated p-values through the Fisher transform).

The deleting method involves the same processes of simulation as the isolating method, however it lets ignore isolated nodes when calculating the values of metrics. We can see that the values of the FC Fitting metric calculated through the deleting method are all positive so that it is easier to interpret them.

Clearly, that the suppression of oscillating nodes with highest bifurcation parameters (HBC) and nodes with highest rate of connectivity (RC) results in the worse values of metrics.

The difference between the freezing and isolating/deleting methods is evident when we compare the values of the FC Fitting metric for the nodes with the lowest bifurcation parameters, producing random close-to-zero time series (LBC). We can see that the value of FC fitting obtained after deleting of these nodes is the least.

This effect may be caused by the significant influence of neighboring nodes upon the LBC nodes. Thus the isolation of the LBC nodes excludes this influence. We can see a general tendency of KS Distance growth with decrease of the FC Fitting metric.

Figure 8 shows the temporal variation of the Kuramoto order parameter for the same ten variants of data.

The exact values of the Mean Synchronization and Metastability metrics are presented in Table 5.

Table 5. Mean Synchronization and Metastability metrics

	FN	BC	RC	LBC	HBC	EMP
Freezing						
Mean Synchronization	0.7621	0.3984	0.3738	0.5287	0.2491	0.5627
Metastability	0.1493	0.1625	0.1615	0.1775	0.1178	0.1938
Isolating						
Mean Synchronization	0.7621	0.8058	0.8209	0.8242	0.3419	0.5627
Metastability	0.1493	0.0370	0.0356	0.0355	0.1423	0.1938

We can see a sufficient influence of the oscillating nodes (HBC) upon the inter-node synchronization. We can also see that isolation, as distinct from freezing, of all groups of nodes except of the HBC nodes raises the level of synchronization.

More simple system with less connections and the same number of oscillating nodes may be more synchronized.

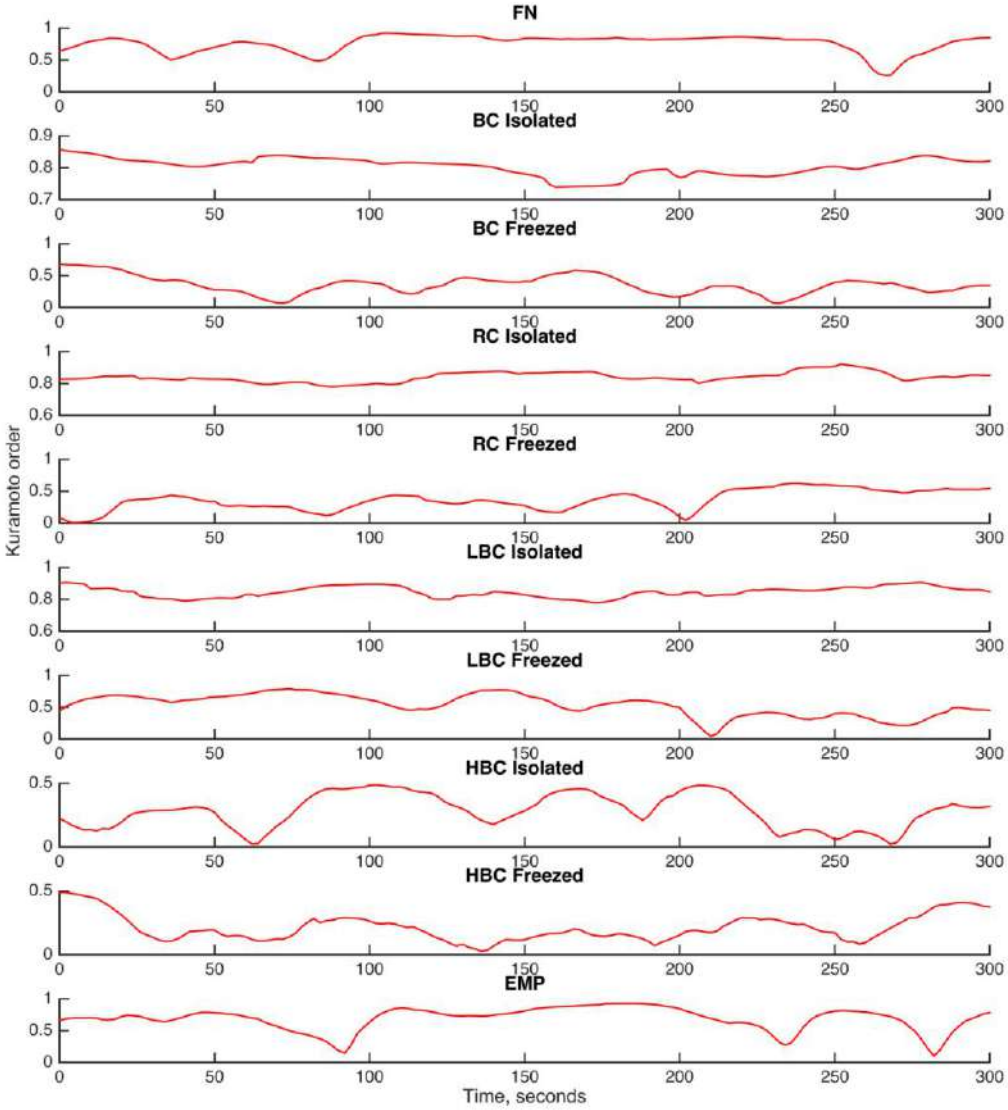

Figure 8. Time history of the Kuramoto order parameter. We used the empirical data for the 24 subjects, similarly we simulated 24 datasets for every group of the suppressed nodes. We displayed graphics of the Kuramoto order parameter within the 300-second periods for the datasets with the highest Metastability metric.

3.3. Results for sequential suppression of nodes

We analyzed alteration of the Mean Synchronization, Metastability and Integration metrics for a sequential suppression of nodes. Thus, we could determine the exact contribution of each node. The nodes were suppressed in an order of descending conformance to the corresponding criteria (from the highest bifurcation parameter for HBC, from the closest to zero bifurcation parameter for BC, etc.). The simulation was performed for 11 variants of the global connectivity parameter G=4.0,4.1,..5.0. Mean values of metrics were calculated. Figures 9 a), b), c) and 10 a), b), c) show the values of the metrics for the freezing and isolating methods respectively.

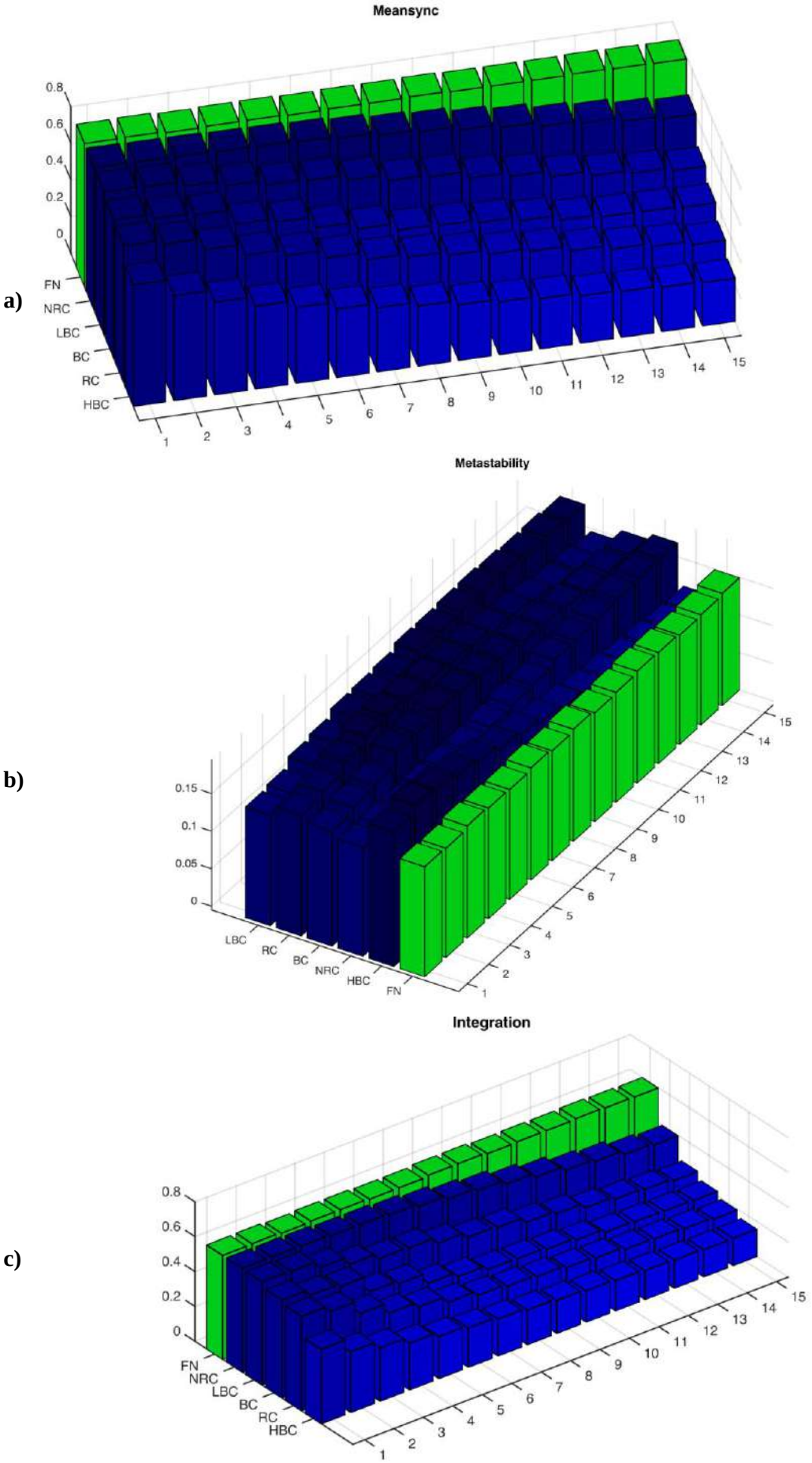

Figures 9 a), b), c). The value of the metrics for the freezing method: a) Mean Synchronization, b) Metastability, c) Integration. We can see monotonous changes in the Mean Synchronization and Integration metrics with equal positions of the node groups (from high to weaker influence: HBC, RC, BC, LBC, NBC) and unessential non-monotonic change in the Metastability metric.

a)

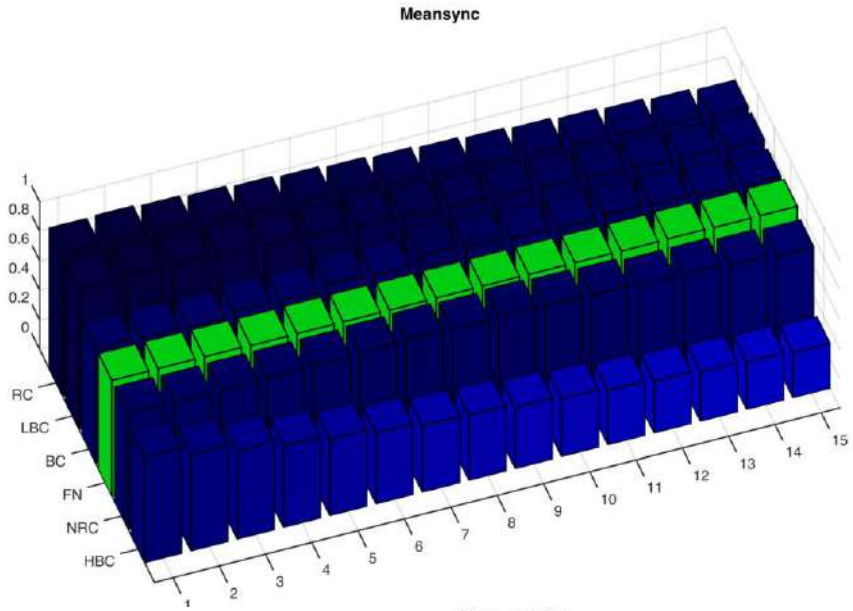

b)

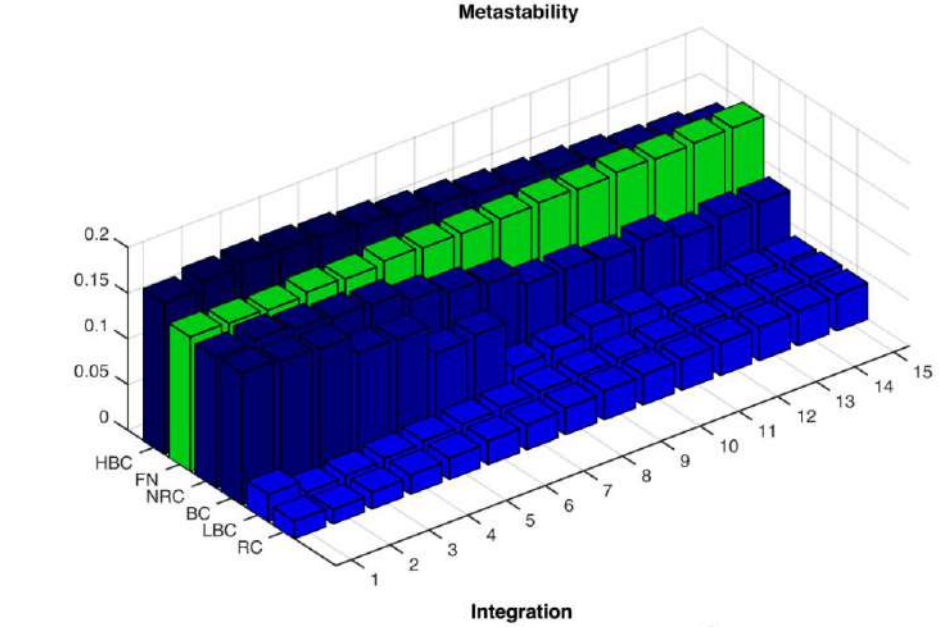

c)

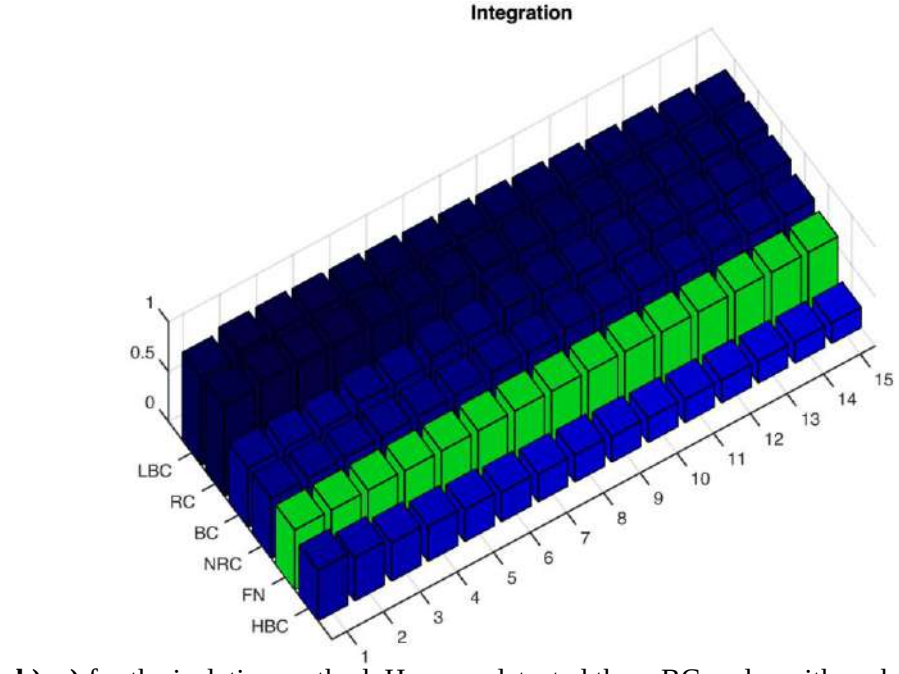

Figures 10 a), b), c) for the isolating method. Here we detected three BC nodes with ranks 4, 6, 8 altering the metrics most significantly when isolated. These nodes refer to the left hemisphere and have the numbers 57, 58, 64 respectively.

We copied out to the Table 6 characteristics of three nodes detected in Figure 10.

Table 6. Characteristics of the nodes matching two criteria

Node Number	Rank *a*	*a*	Rank |*a*|	|*a*|	Rank *c*	*c*
57	34	-0.0475	6	0.0475	63	0.7218
58	35	-0.0290	4	0.0290	57	0.5370
64	33	-0.0703	8	0.0703	55	0.5154

We can see that the nodes match two criteria of nodes selection: their bifurcation parameters are close to zero and the connectivity rate is high.

3.4. Experiments with nodes matching two criteria

We examined if the freezing of the two-criteria nodes would result in essential change of the model metrics. We obtained essential positive results for the node 58 combined with the symmetrical node 24 referring to the right hemisphere. The pair (24; 58) corresponds to precunens cortex (PC) (see Fig.11).

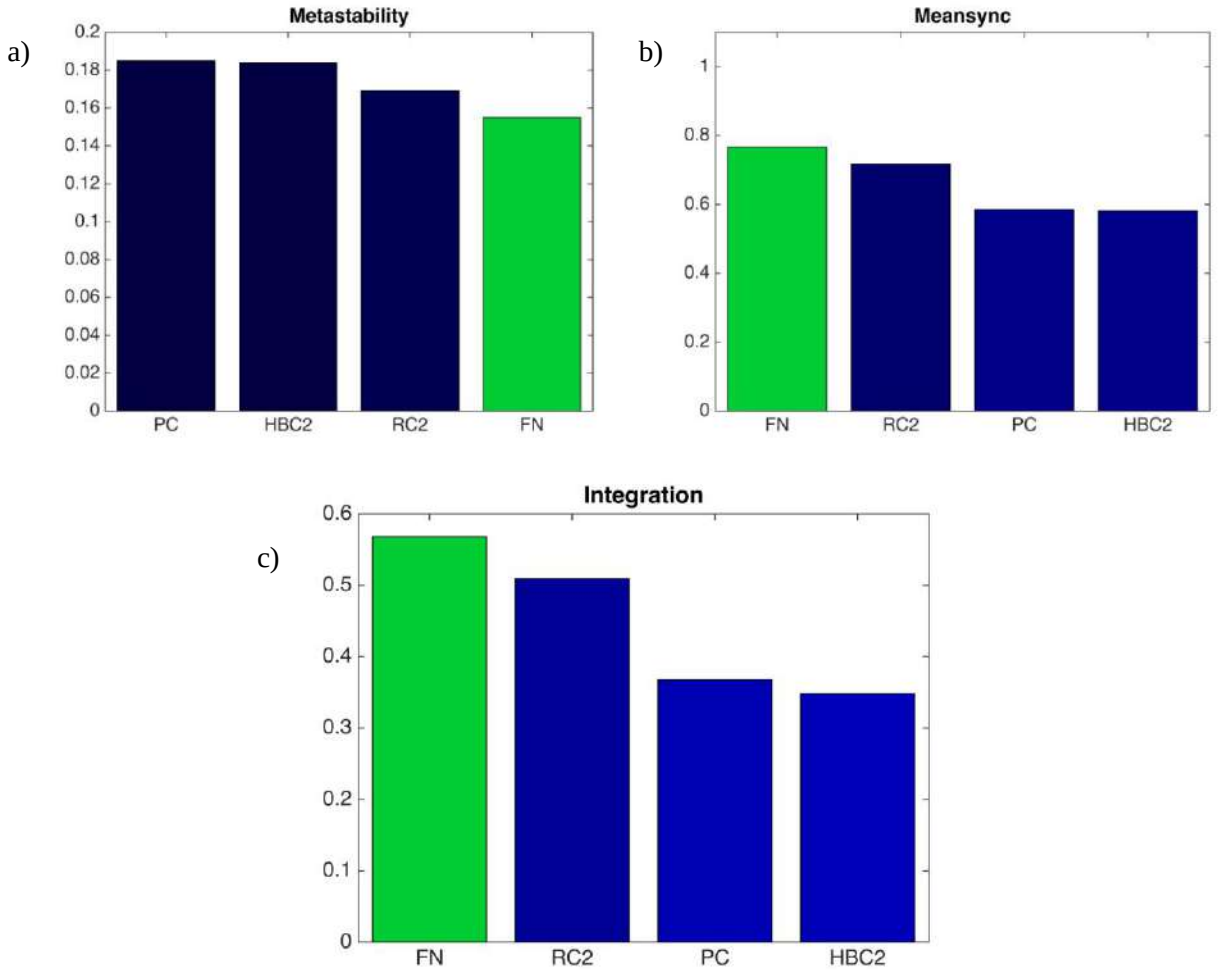

Figures 11 a) Mean synchronization, b) Metastability, c) Integration. The values of metrics for precuneus cortex (PC) (nodes 24, 58), two nodes with the highest bifurcation parameters (HBC2) and two nodes with the highest rate of connectivity (RC2). We can see the effect of PC nodes equal to that of HBC2.

4. Discussion

4.1. Capabilities of the nodes suppression methods

Comparison of the results obtained via two methods, namely freezing and isolating, lets analyze different aspects of spatial and temporal patterns emergence in the resting-state brain activity. More specifically, the isolating method, as distinct from the freezing method, blocks the influence of the other nodes upon the isolated node and prevents a transition of signals through this node.

4.2. Coherent activities in right and left hemispheres in a resting state

The data used for the model construction (connectivity of brain regions, spectrums of BOLD signals) could not explain high functional connectivity between symmetrical regions in right and left hemispheres. Two links to the models symmetry: close values of bifurcation parameters and identical connectivity levels in symmetrical nodes do not result in the high functional connectivity.

4.3. Roles of different brain regions in emergence of spatial and temporal patterns in a resting-state brain activity

A performance of nodes representing different brain regions gives a link to understanding the emergence of spatial and temporal patterns in a resting-state brain activity.

The most prominent in all patterns are the oscillating nodes with high bifurcation parameters. These nodes are necessary for the inter-node synchronization.

Less critical are nodes with a high connectivity rate. These nodes have an ability of intensive communication with their neighborhood.

The nodes with the lowest bifurcation parameters (high negative) appeared to be good recipients of signals from the other nodes.

We detected two-criteria nodes (with bifurcation parameters close to zero and high connectivity rate) that may have a critical role in transmitting signals between the other nodes.

The most significant effect in inter-node synchronization was obtained for the pairs of nodes representing the regions of *precuneus cortex* in right and left hemisphere. The node representing precuneus cortex in the left hemisphere appeared to be the most typical two-criteria node.

4.4. Direction for future research

Two aspects should be investigated more thoroughly: first, the significance of the functional connectivity between symmetrical brain regions in right and left hemispheres for simulation of the resting-state activity; second, the transit inter-node communications through intermediate nodes, specifically, the influence of node characteristics on its ability to transmit signal between other nodes.

5. Conclusion

Alternative methods of nodes suppression in a whole brain model provide us with results revealing the roles of different brain regions in the emergence of spatial and temporal patterns in the resting-state brain activity. Particularly, we distinguished critical nodes in generation of coherent behavior and in transmitting inter-node signals.

Future refinement of the model may be concerned with accounting of functional connectivity between the symmetrical brain regions in right and left hemispheres.

References

Alan, V. Oppenheim and Ronald W. Schafer, Discrete-Time Signal Processing, 2nd ed., Prentice-Hall, Upper Saddle River, New Jersey, 1998.

Basser, P. J. and C. Pierpaoli (1996). "Microstructural and physiological features of tissues elucidated by quantitative-diffusion-tensor MRI." J Magn Reson B111(3): 209-219.

Beaulieu, C. (2002). "The basis of anisotropic water diffusion in the nervous system - a technical review." NMR Biomed15(7-8): 435-455.

Biswal, B., F. Z. Yetkin, V. M. Haughton and J. S. Hyde (1995). "Functional connectivity in the motor cortex of resting human brain using echo-planar MRI." Magn.Reson.Med.34: 537-541.

Butterworth, S. (1930) "On the Theory of Filter Amplifiers". In Wireless Engineer (also called Experimental Wireless and the Wireless Engineer), vol. 7, 1930, pp. 536–541.

Cabral, J., Kringelbach M. L., Deco, G. (2014) "Exploring the network dynamics underlying brain activity during rest". Progress in Neurobiology 114: 102–131.

Deco, G., Hagmann, P., Hudetz, A.G., Tononi, G., 2013a. Modeling resting-state functional networks when the cortex falls sleep: local and global changes. Cereb Cortex, [Epub ahead of print].

Deco, G., V. K. Jirsa and A. R. McIntosh (2011). "Emerging concepts for the dynamical organization of resting-state activity in the brain." Nat Rev Neurosci12(1): 43-56.

Deco, G., V. K. Jirsa and A. R. McIntosh (2013b). "Resting brains never rest: computational insights into potential cognitive architectures." Trends Neurosci36(5): 268-274.

Freyer, F., J. A. Roberts, P. Ritter and M. Breakspear (2012). "A canonical model of multistability and scale-invariance in biological systems." PLoS Comput Biol8(8): e1002634.

Freyer, F., J. A. Roberts, R. Becker, P. A. Robinson, P. Ritter and M. Breakspear (2011). "Biophysical mechanisms of multistability in resting-state cortical rhythms." J Neurosci31(17): 6353-6361.

Hagmann, P., L. Cammoun, X. Gigandet, S. Gerhard, P. Ellen Grant, V. Wedeen, R. Meuli, J. P. Thiran, C. J. Honey and O. Sporns (2010). "MR connectomics: Principles and challenges." J Neurosci Methods194(1): 34-45.

Hansen, E. C., D. Battaglia, A. Spiegler, G. Deco and V. K. Jirsa (2015). "Functional connectivity dynamics: Modeling the switching behavior of the resting state." Neuroimage105: 525-535.

Johansen-Berg, H. and M. F. Rushworth (2009). "Using diffusion imaging to study human connectional anatomy." Annu Rev Neurosci32: 75-94.

Ritter, P., M. Schirner, A. R. McIntosh and V. K. Jirsa (2013). "The virtual brain integrates computational modeling and multimodal neuroimaging." Brain Connect3(2): 121-145.

Schirner, M., S. Rothmeier, V. Jirsa, A. R. McIntosh and P. Ritter "Constructing subject-specific virtual brains from multimodal neuroimaging data." (Neuroimage, first revision).

Smith, Steven W. (1997) "The Scientist and Engineer's Guide to Digital Signal Processing". California Technical Pub.; 1st edition: 626 p.

Wand, M. P. and Jones, M. C. (1995). Kernel Smoothing, Vol. 60 of Monographs on Statistics and Applied Probability, Chapman and Hall, London.

Wildie, M. and M. Shanahan (2012). "Metastability and chimera states in modular delay and pulse-coupled oscillator networks." Chaos22(4): 043131.

Annex 1

	Grand_Average	MS_Effect	MS_Error	F
1	9.8020e+03	3.4163e+08	3.3984e+03	1.0052e+05
2	1.1584e+04	3.4692e+08	4.7478e+03	7.3070e+04
3	1.0638e+04	7.3854e+08	2.7991e+03	2.6385e+05
4	1.0988e+04	1.0215e+09	8.1503e+03	1.2534e+05
5	4.7156e+03	1.9724e+09	2.5494e+03	7.7367e+05
6	7.6952e+03	5.7253e+08	2.4385e+03	2.3479e+05
7	1.0501e+04	1.1676e+09	2.4786e+03	4.7106e+05
8	5.9113e+03	7.5289e+08	1.3458e+03	5.5944e+05
9	1.0417e+04	1.1656e+08	7.1351e+03	1.6336e+04
10	9.8421e+03	1.5756e+09	5.6631e+03	2.7822e+05
11	7.6426e+03	7.7009e+08	3.4694e+03	2.2197e+05
12	9.9704e+03	2.8180e+08	8.0228e+03	3.5125e+04
13	8.0323e+03	7.4205e+08	2.6002e+03	2.8539e+05
14	7.7040e+03	7.9627e+08	1.2926e+03	6.1603e+05
15	8.3019e+03	3.8424e+08	2.6436e+03	1.4535e+05
16	1.0556e+04	4.6355e+08	4.4027e+03	1.0529e+05
17	1.1546e+04	9.7313e+08	3.2084e+03	3.0331e+05
18	8.7424e+03	1.3313e+09	9.9567e+03	1.3371e+05
19	1.1443e+04	1.0856e+09	5.4422e+03	1.9949e+05
20	1.1367e+04	9.2723e+08	1.3426e+04	6.9063e+04
21	9.1516e+03	3.8805e+08	2.8032e+03	1.3843e+05
22	1.0986e+04	1.4956e+08	3.4565e+03	4.3271e+04
23	1.0038e+04	5.0838e+08	2.4499e+03	2.0751e+05
24	1.1204e+04	3.4269e+08	4.3454e+03	7.8864e+04
25	1.1254e+04	4.7214e+08	3.6247e+03	1.3026e+05
26	1.1254e+04	7.5598e+08	3.2180e+03	2.3493e+05
27	1.1103e+04	3.8916e+08	2.4459e+03	1.5911e+05
28	1.0476e+04	1.0746e+09	3.8973e+03	2.7574e+05
29	9.4058e+03	5.7233e+08	1.9425e+03	2.9463e+05
30	9.6485e+03	3.9961e+08	1.8664e+03	2.1411e+05
31	3.8121e+03	3.1494e+09	8.3635e+03	3.7657e+05
32	5.9685e+03	2.8274e+09	2.2636e+03	1.2491e+06
33	9.5697e+03	2.5048e+08	5.3946e+03	4.6432e+04
34	1.1088e+04	5.4893e+08	2.7235e+03	2.0155e+05
35	1.3018e+04	8.3109e+08	7.2073e+03	1.1531e+05
36	1.1877e+04	2.3048e+08	4.2311e+03	5.4474e+04
37	1.0753e+04	7.1551e+08	2.8799e+03	2.4845e+05
38	1.0762e+04	1.1211e+09	9.4110e+03	1.1913e+05
39	4.4709e+03	2.4603e+09	3.3043e+03	7.4458e+05
40	8.4004e+03	6.5809e+08	3.8761e+03	1.6978e+05
41	1.2790e+04	1.2273e+09	3.7601e+03	3.2640e+05
42	6.6541e+03	9.8599e+08	2.3211e+03	4.2480e+05
43	1.0531e+04	1.6130e+08	6.1483e+03	2.6234e+04
44	1.0560e+04	1.7193e+09	7.5782e+03	2.2687e+05
45	7.3069e+03	4.4757e+08	3.1844e+03	1.4055e+05
46	1.0085e+04	3.9760e+08	1.0312e+04	3.8557e+04
47	8.6819e+03	4.4462e+08	2.9086e+03	1.5286e+05
48	9.3504e+03	4.9723e+08	2.0000e+03	2.4861e+05
49	8.6459e+03	6.8982e+08	3.8835e+03	1.7763e+05
50	1.0713e+04	5.7642e+08	4.3814e+03	1.3156e+05
51	1.1165e+04	3.2449e+08	3.2816e+03	9.8882e+04
52	8.1547e+03	7.8020e+08	6.1778e+03	1.2629e+05
53	1.0314e+04	3.5059e+08	3.7589e+03	9.3269e+04
54	1.1324e+04	1.1038e+09	1.6596e+04	6.6512e+04
55	1.1656e+04	1.6846e+09	5.4748e+03	3.0769e+05
56	1.1192e+04	2.2308e+08	3.3204e+03	6.7184e+04
57	1.1112e+04	1.1464e+09	3.5456e+03	3.2333e+05
58	1.1437e+04	3.6789e+08	5.0196e+03	7.3292e+04
59	1.1721e+04	5.1911e+08	3.8389e+03	1.3522e+05
60	1.1228e+04	5.7967e+08	3.3005e+03	1.7563e+05
61	1.1426e+04	2.6939e+08	2.3159e+03	1.1632e+05
62	1.1590e+04	1.1069e+09	5.2914e+03	2.0920e+05
63	1.0740e+04	3.9061e+08	3.0356e+03	1.2868e+05
64	1.3418e+04	1.4677e+09	4.4312e+03	3.3123e+05
65	4.1380e+03	2.9209e+09	7.6151e+03	3.8357e+05
66	5.5414e+03	3.5742e+09	2.5993e+03	1.3751e+06
67	1.1834e+04	5.3714e+08	7.3146e+03	7.3435e+04
68	1.1500e+04	2.0259e+08	3.1714e+03	6.3882e+04

Figure 1. One-way ANOVA results describing difference between subjects' BOLD signal series. Numbers of rows (1 … 68) correspond to numbers of brain regions. "Grand Average" is an average level of a signal (at a given region) calculated for all frames (for all the 661 time points) and for all the 24 subjects. "MS-effect" shows mean squares for inter-subject differences, it is equal to inter-group variance expressing a variation of mean signal levels for different subjects. Similarly "MS-Error" (mean squares for frames differences within individual time series) is equal to a total variance not associated with inter-subject differences. "F" (F-statistic) is a ratio of "MS-effect" to "MS-error". "F" follows F-distribution with (24-1, 661x24-24)=(23, 15840) degrees of freedom. For all brain regions p-values calculated by F-statistics could not be distinguished from 0, hence the inter-subject differences are highly significant.

Annex 2

The one-way filtering through a four-order Butterworth filter produced an output signal for a set of previous sequential values according to the following recurrence equation:

$$y(n)=b_0x(n)+ b_2x(n-2)+ b_4x(n-4) – a_1y(n-1) – a_2y(n-2) – a_3y(n-3) – a_4y(n-4), \quad (1)$$

where $b_0 \ldots b_4>0$ are numerator coefficients and $a_0 \ldots a_4>0$ are denominator coefficients.

For describing a bi-directional filtering process a symmetrical form of the equation is more convenient:

$$b_0x(n)+ b_2x(n-2)+ b_4x(n-4) = a_0y(n) + a_1y(n-1) + a_2y(n-2) + a_3y(n-3) + a_4y(n-4), \quad (2)$$

where $a_0=1$.

Thus, we calculated the output time series *y* for the input time series *x*. Then we performed a backward filtering for *y* calculating an output time series *z* through a set of future sequential signals. For example, we may obtain $z(n-4)$ through $y(n-3) \ldots y(n)$ and $z(n-3) \ldots z(n)$:

$$b_0y(n-1)+ b_2y(n-2)+ b_4y(n) = a_0z(n-4) + a_1z(n-3) + a_2z(n-2) + a_3z(n-1) + a_4z(n), \quad (3)$$

where all coefficients are the same as in the previous equation.

The backward filtering compensated the phase distortion, so we got a zero-phase shift as compare *z* and *x*. The responses of the one-way and bi-directional filtering are shown at Figure 2.

To get a single-sided amplitude spectrum we applied a Fourier transform to the filtered signals and got a magnitude:

$$Z(k)=|\sum_{n=1..N} z(n)*exp(-i*2\pi*(k-1)*(n-1)/N)|, \quad (4)$$

where $Z(k)$ is an amplitude for the frequency number k, $1<=k<=N$.

The frequencies were enumerated with the step of 1/(661*2), where 661 is number of frames (one frame recoded per two seconds).

We performed a kernel smoothing (Wand and Jones, 1995) of the power spectrums to exclude random peaks. In a kernel smoothing the resulting value at a given point is calculated via a weighted sum of values at neighboring points the weights are defined by a kernel function. We used the Gauss kernel (the density of normal distribution) sigma equal to 0.01.

Figure 2. One way and bi-directional filtering responses for the bandpass Butterworth filters.
The graphics show the amplitude and phase responses for the one-way and bi-directional filtering. The logarithmic scale was used for the amplitude response. The axis of abscises shows normalized frequencies 0…1 (real frequencies were divided by the Nyquist frequency). The bi-directional filtering produced nearly the same amplitude flat response for the bandpass frequencies and more sharp decline at the bandstop frequencies.

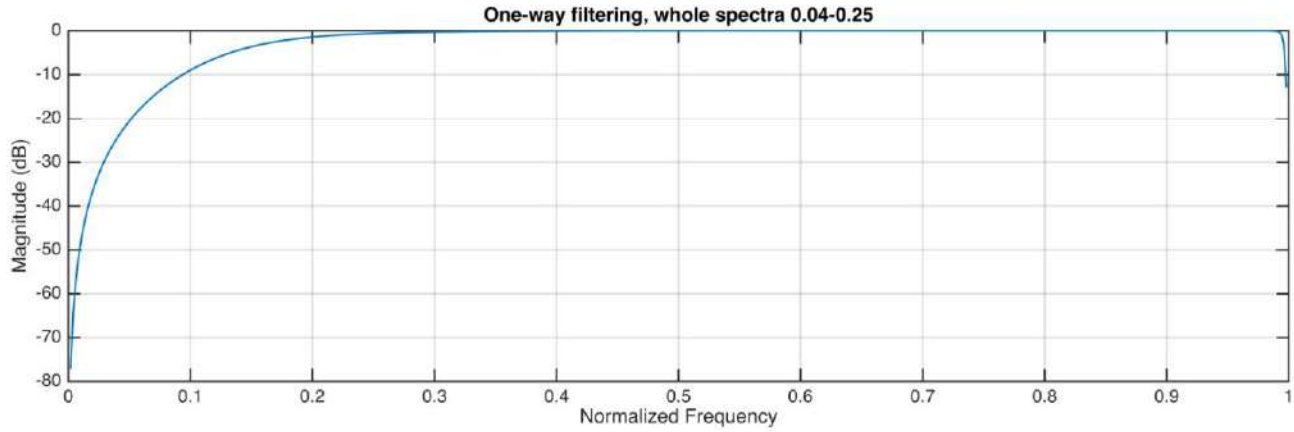
One-way filtering, whole spectra 0.04-0.25
Magnitude (dB)
Normalized Frequency

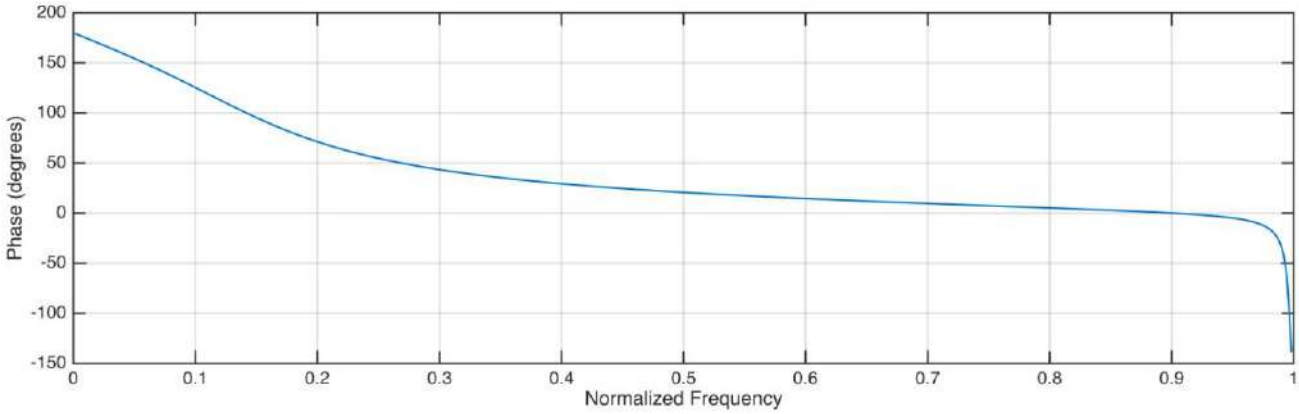
Phase (degrees)
Normalized Frequency

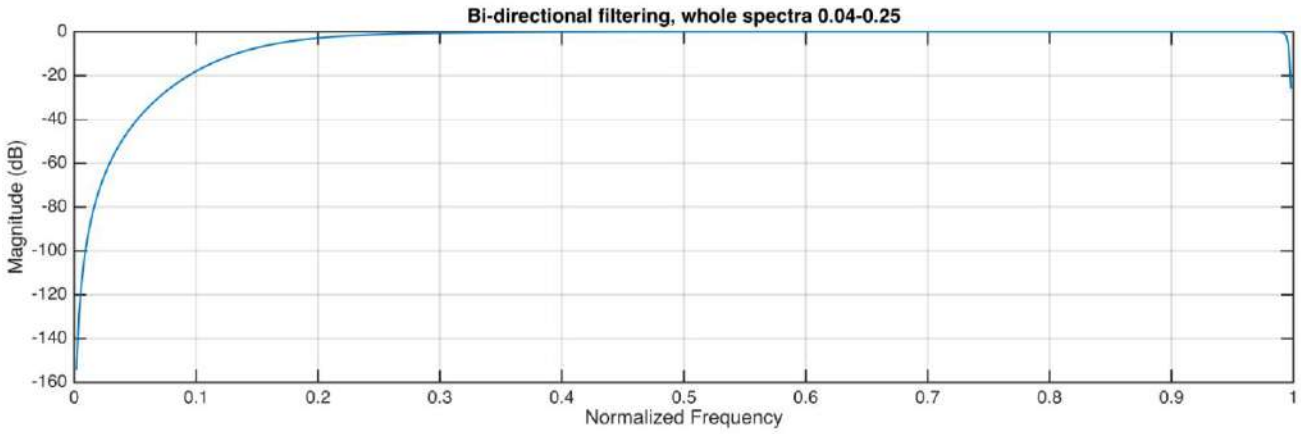
Bi-directional filtering, whole spectra 0.04-0.25
Magnitude (dB)
Normalized Frequency

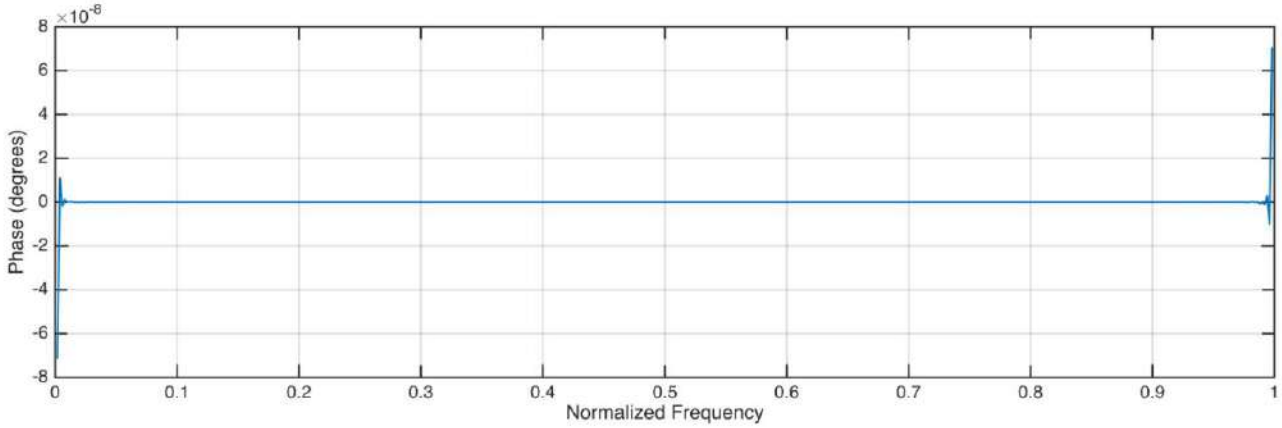
×10^-8
Phase (degrees)
Normalized Frequency

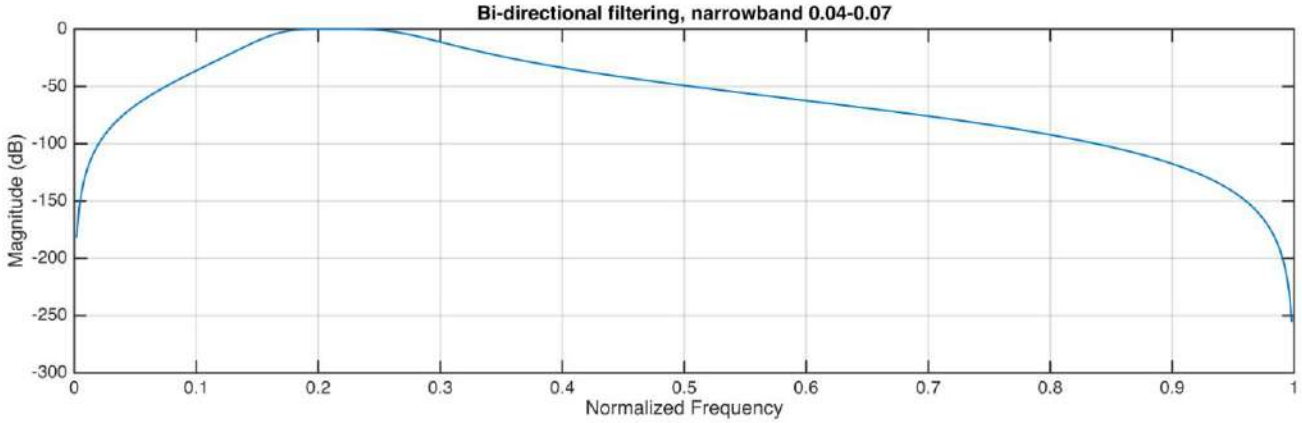
Bi-directional filtering, narrowband 0.04-0.07
Magnitude (dB)
Normalized Frequency

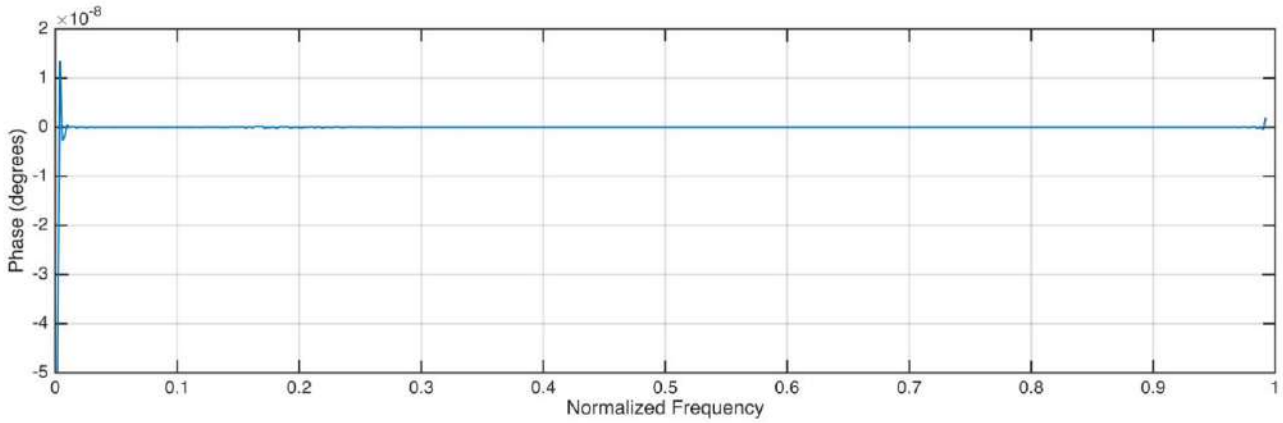
×10^-8
Phase (degrees)
Normalized Frequency

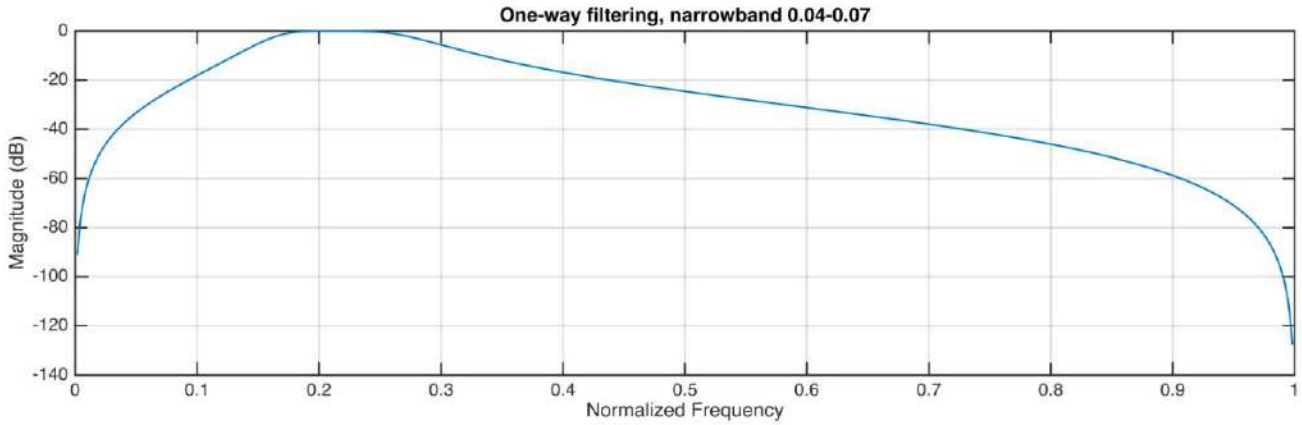
One-way filtering, narrowband 0.04-0.07
Magnitude (dB)
Normalized Frequency

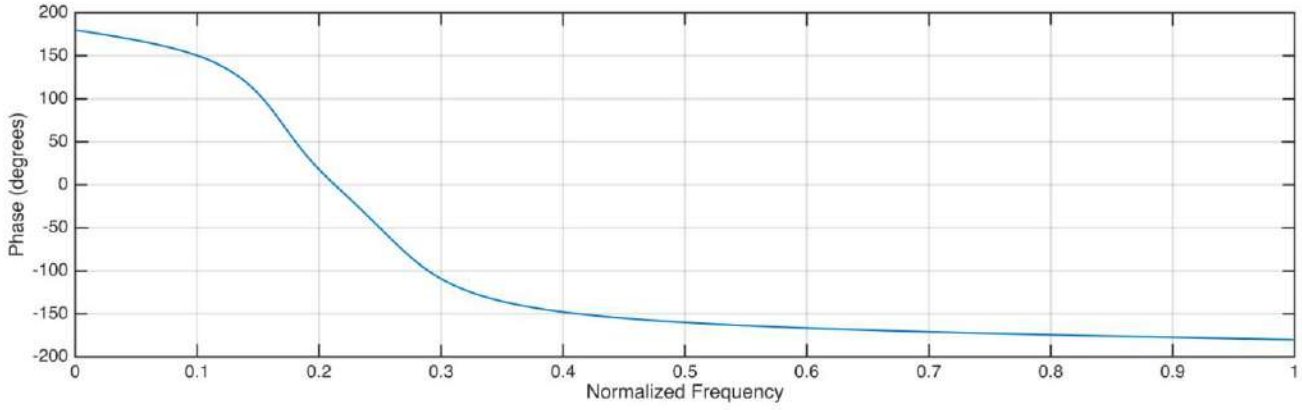
Phase (degrees)
Normalized Frequency